Semi-automated tracking of iceberg B43 using Sentinel-1 SAR images via Google Earth Engine

5   YoungHyun Koo[1], Hongjie Xie[1], Stephen F. Ackley[1], Alberto M. Mestas-Nuñez[1], Grant J. Macdonald[1], Chang-Uk Hyun[2]

[1] NASA MIRO Center for Advanced Measurements in Extreme Environments (CAMEE), University of Texas at San Antonio, San Antonio, TX 78249, USA

[2] Department of Energy and Mineral Resources Engineering, Dong-A University, Busan 49315, Republic of Korea

10 *Correspondence to*: Hongjie Xie (Hongjie.Xie@utsa.edu)

Abstract. Sentinel-1 C-band synthetic aperture radar (SAR) images can be used to observe the drift of icebergs over the Southern Ocean with around 1-3 days of temporal resolution and 10-40 m of spatial resolution. The Google Earth Engine (GEE) cloud-based platform allows processing of a large quantity of Sentinel-1 images, saving time and computational resources. In this study, we

15 process Sentinel-1 data via GEE to detect and track the drift of iceberg B43 during its lifespan of 3 years (2017-2020) in the Southern Ocean. First, to detect all candidate icebergs in Sentinel-1 images, we employ an object-based image segmentation (simple non-iterative clustering – SNIC) and a traditional backscatter threshold method. Next, we automatically choose and trace the location of the target iceberg by comparing the centroid distance histograms (CDHs) of all detected icebergs in subsequent days with the CDH of the reference target iceberg. Using this approach, we successfully track the iceberg B43 from the Amundsen

20 Sea to the Ross Sea, and examine its changes in area, speed, and direction. Three periods with sudden losses of area (i.e. split-offs) coincide with periods of low sea ice concentration, warm air temperature, and high waves. This implies that these variables may be related to mechanisms causing the split-off of the iceberg. Since the iceberg is generally surrounded by compacted sea ice, its drift correlates in part with sea ice motion and wind velocity. Given that the bulk of the iceberg is under water (~30-60 m freeboard and ~150-400 m thickness), its motion is predominantly driven by the westward-flowing Antarctic Coastal Current (ACoC) which

25 dominates the circulation of the region. Considering the complexity of modeling icebergs, there is a demand for a large iceberg database to better understand the behavior of icebergs and their interactions with surrounding environments. The GEE-based semi-automated iceberg tracking method presented here can be used for this purpose.

1. Introduction

30

When a large ice mass breaks off from an ice shelf or glacier into the ocean, it forms an iceberg. An iceberg has a lifespan of several years or longer and its area ranges from a few square kilometers to thousands of square kilometers. Since the majority of an iceberg is under water, iceberg drift is a good indicator of ocean circulation (Collares et al., 2018). In addition, the formation and melting of icebergs influences global climate (Romanov et al., 2008), ocean flux (Silva et al., 2006; Rackow et al., 2017; Starr

35 et al., 2021), sea ice production (Martin et al., 2007; Merino et al., 2016), and ecosystems and biology (Wilson et al., 2016; Schwarz and Schodlok, 2009; Biddle et al., 2015). Furthermore, icebergs can threaten ship navigation (Lasserre, 2015)**.** Therefore, detecting and tracking icebergs is extremely important.

Radar remote sensing is an efficient tool for monitoring both movements and area changes of icebergs. While multispectral images can be useful for observing icebergs, they cannot be used during polar night or under cloudy conditions. In

40 contrast, synthetic aperture radar (SAR) images can be used for analysis regardless of the weather conditions or time of year (Han et al., 2019; Mazur et al., 2017; Wesche and Dierking, 2012). Indeed, various SAR instruments have been used for detecting or tracking icebergs in the polar oceans including ERS-1 (Young et al., 1998; Willis et al., 1996), ENVISAT (Li et al., 2018; Howell et al., 2004; Mazur et al., 2017), Radarsat-1 (Wesche and Dierking, 2015; Lane et al., 2002; Power et al., 2001), Radarsat-2 (Scheuchl et al., 2004; Denbina and Collins, 2014), TerraSAR-X (Frost et al., 2016), and Sentinel-1 (Lopez-Lopez et al., 2020;

45 Moctezuma-Flores and Parmiggiani, 2017; Heiselberg, 2020; Han et al., 2019).

Sentinel-1 has been popular for iceberg detection since the launch of Sentinel-1 A and B in 2014 and 2016, respectively, because of its remarkable temporal and spatial resolution. Since each satellite has a 12-day revisit cycle, the constellation of the two satellites (Sentinel-1 A/B) can have a revisit cycle of 6 days. Moreover, because the coverage is more frequent at high latitudes in the Southern Ocean, one can acquire Sentinel-1 data with a temporal resolution of at least 2-3 days (Torres et al., 2012). Sentinel-

50 1 also has a high spatial resolution ($\leq$ 40 m depending on resolution modes), enabling resolution of icebergs and iceberg features at a fine spatial scale.

Another advantage of Sentinel-1 data is that it is non-commercial and freely accessible via Google Earth Engine (GEE), a cloud computing platform for geospatial analysis by Google (Gorelick et al., 2017). GEE makes it possible to process a large volume of geospatial data without downloading them onto local computers. A number of studies have taken advantage of the

55 unprecedented computing performance of GEE for Sentinel-1 data processing: glacier margin mapping (Lea, 2018), glacier lake mapping (Zhang et al., 2020), estimation of glacier surface speed (Di Tullio et al., 2018), crop mapping (Mandal et al., 2018; Singha et al., 2019; Jin et al., 2019), flood mapping (DeVries et al., 2020; Clement et al., 2018), and wetland mapping (Mahdianpari et al., 2019, 2020). Despite the variety of applications of Sentinel-1 data in the GEE platform, there have not yet been any published studies that leverage GEE's large data storage capabilities and computing power for automatic tracking of icebergs.

60

In this study, we track the drift of an iceberg in the Southern Ocean by taking advantage of the Sentinel-1 data and the GEE platform. Our target iceberg is the iceberg B43, as designated by the National Ice Center (NIC, usicecenter.gov), which calved off from the Thwaites Glacier ice shelf in the Amundsen Sea in April 2017 (Figure 1). This tabular iceberg had a relatively large size (> 100 km^2 in April 2017) and a distinctive shape compared to surrounding icebergs. It drifted westward along the coast from the Amundsen Sea to the Ross Sea with a relatively stable flat-topped surface and eventually broke into several pieces in the

65 northern Ross Sea in March 2020. Since the iceberg has a distinctive shape that facilitates its identification, we were able to trace its entire journey. The aim of this study is to track the drift and decay of this iceberg from the Amundsen Sea to the Ross Sea and to assess the impact of major environmental factors (e.g. ocean currents, winds, sea ice concentration, sea ice drift, temperature) on changes in its movement and area. In addition, we examine satellite altimeter data to estimate the freeboard and thickness of this iceberg.

70
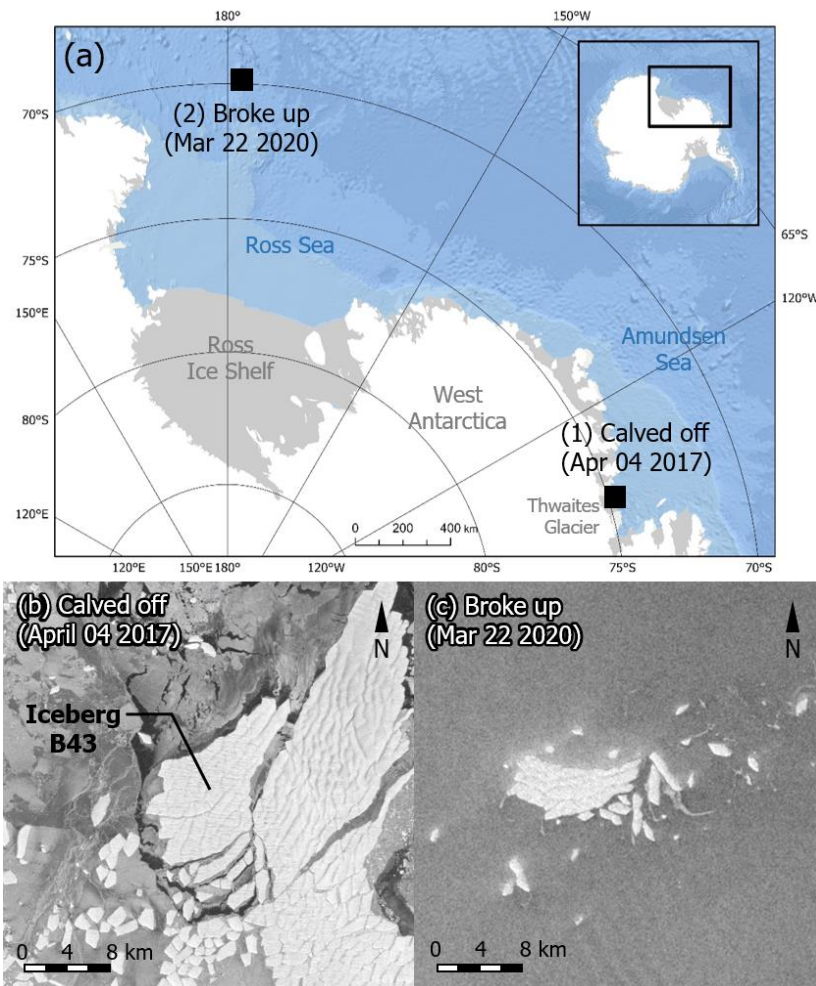
Figure 1. (a) Expanded map of the Antarctic region showing the locations where iceberg B43 (1) calved off in the Amundsen Sea (April 04, 2017) and (2) broke up in the Ross Sea (March 22, 2020). (b) Sentinel-1 SAR image showing the ice conditions when B43 calved off and (c) Sentinel-1 SAR image showing the ice and ocean conditions when B43 broke up; waves are observed in the vicinity of the iceberg.

75

2. Data

2.1. Sentinel-1 SAR images

In this study, we use ESA's Sentinel-1 C-band (center frequency of 5.405 GHz, wavelength of 5.6 cm) SAR Ground

80   Range Detected (GRD) data in order to detect the location and area of the target iceberg. This product has three different spatial resolutions of 10, 25, or 40 meters with different resolution modes, but all images are resampled to 40 m. We import and process these images via the GEE Code Editor (web-based integrated development environment (IDE) for the GEE JavaScript API) and GEE Python API. Each Sentinel-1 image scene is released from ESA after being pre-processed with (1) thermal noise removal, (2) radiometric calibration, and (3) terrain correction (sentinel.esa.int). Of four available band combinations of the polarization

85   products (VV, HH, VV+VH, and HH+HV), we use only the HH band because most of the images contain this band. In addition,

we also use the angle band that represents the interpolated viewing incidence angle at each cell. During the automated tracking of the iceberg, a total of 433 images from April 2017 to March 2020 are used.

2.2. Satellite altimeter data

90   In order to estimate the freeboard and thickness of the iceberg, we use height measurements from two satellite altimeters: CryoSat-2 and ICESat-2.

CryoSat-2 employs Ku band radar (center frequency of 13.575 GHz) to measure surface heights with 400 m of along track footprint and 1.65 km of across track footprint. It operates in SAR mode over sea ice and oceanographic areas and SAR Interferometric (SIN) mode around ice sheet edges and mountain glaciers (ESA, 2019). Since the target iceberg floated in the ocean through sea ice and coastal areas, we search for both Level 2 SAR and SIN products that overlapped with the iceberg from April

95   2017 to March 2020.

ICESat-2's Advanced Topographic Laser Altimeter System (ATLAS) uses laser photons at 532 nm to retrieve surface heights with 17 m of laser footprint and 0.7 m of spacing. Trillions of photons are emitted for each pulse but the number of returned photons is around seven photons for a typical snow-covered surface (Neumann et al., 2019). ATLAS consists of six multi-beams, each with three strong beams and three weak beams, and the strong beams have four times greater energy than the weak beams

100   (Markus et al., 2017; Neumann et al., 2019). We search for ICESat-2 ATL03 geolocated photon products (release 003) (Neumann et al., 2020) that intersected the iceberg during our study period.

2.3. Meteorological and sea ice motion data

We compare the drift speed, direction, and area changes of the iceberg with meteorological data from the European Centre for Medium-Range Weather Forecasts (ECMWF) ERA5 reanalysis model. We use the 2m air temperature, sea ice concentration

105   (SIC), wind speed/direction, and wave height from the ERA5 hourly product, which has a spatial resolution of about 0.25°. This product was acquired from the Climate Data Store (cds.climate.copernicus.eu) of the Copernicus Climate Change Service.

In addition, we acquire National Snow and Ice Data Center (NSIDC) sea ice motion vector data (nsidc.org/data/NSIDC-0116) (Tschudi et al., 2019). This dataset contains daily sea ice motion vectors, which are derived from multiple data sources, including AVHRR, AMSR-E, SMMR, SSMI, and SSMI/S sensors, International Arctic Buoy Program (IABP) buoys (in the Arctic

110   only), and National Center for Environmental Prediction (NCEP) and National Center for Atmospheric Research (NCAR) Reanalysis forecasts. These sea ice motions are projected to the 25 km EASE (Equal-Area Scalable Earth)-Grid.

3. Method

3.1. Iceberg detection

115   To detect the target iceberg from the Sentinel-1 images, we employ a superpixel image segmentation method named simple non-iterative clustering (SNIC) (Achanta and Süsstrunk, 2017). This approach uses a similar concept to k-means based clustering (Simple Linear Iterative Clustering (SLIC) algorithm (Achanta et al., 2012)), but in contrast with SLIC, SNIC enforces connectivity from the start. Since GEE provides this SNIC algorithm as a basic built-in function, we use the SNIC function in the GEE environment. The object-based segmentation processes of SNIC in this study are summarized by the following steps:

120

(i) Apply Gaussian filter to the raw SAR image

The speckle effects of the original SAR images can introduce errors (Figure 2a). In particular, the image segmentation

process can misinterpret shaded areas associated with the iceberg surface topography as artificial iceberg boundaries and split the iceberg into several pieces. To reduce this effect, we first smooth images by applying a Gaussian filter kernel within a 3-pixel radius (Figure 2b).

(ii) Initialize superpixels

In the SNIC image segmentation, all image pixels should be grouped into small clusters of connected pixels, which are named superpixels. The centroids of superpixels, referred to as seeds, are initialized with a given number of pixels chosen *a priori* on a regular grid. The size of each segment is determined by the seed value. A smaller seed value can distingush small icebergs but takes a longer computation time (Figure 2c); a larger seed value cannot distinguish small icebergs but can reduce computation time (Figure 2d). As shown in Figure 2d, considering the size of the target iceberg, a seed value of 80 (i.e. initial centroid is spaced by 80 pixels) is adequate to detect the target iceberg B43.

(iii) Measure affinity to a centroid

The affinity of the *j*-th pixel to the *k*-th superpixel centroid is calculated by using the distance between them ($d_{j,k}$):

$$d_{j,k} = \sqrt{\frac{\|X_j - X_k\|^2}{s} + \frac{\|C_j - C_k\|^2}{m}} \qquad (1)$$

where X_j is a geocoordinate (latitude and longitude) of the *j*-th pixel, X_k is a geocoordinate of the *k*-th superpixel centroid, C_j is the HH band backscatter of the *j*-th pixel, C_k is the HH band backscatter of the *k*-th superpixel centroid, and *s* and *m* are the normalizing factors for spatial and backscatter distance, respectively. If an image has N pixels and K superpixels are expected, *s* in Equation 1 should be set to $\sqrt{N/K}$. A higher compactness factor *m* leads to more compacted superpixels and poorer boundary adherence (Achanta and Süsstrunk, 2017), and we set *m* equal to 1.

(iv) Evolution of centroid

Contrary to multiple iterations of SLIC (Achanta et al., 2012), SNIC uses a priority queue to choose the next pixel to be added to a cluster. The priority queue consists of multiple candidate pixels that are 8-connected to a currently growing superpixel cluster. The pixel candidate that has the smallest distance from a centroid is selected among these pixel candidates, and the centroid value is updated online after a new pixel is added to that superpixel. This allows the SNIC algorithm to complete the updating of centroids in a single iteration with lower memory requirements. More details about the SNIC algorithm were explained in Achanta and Süsstrunk (2017).

After completing the SNIC image segmentation, we detect the segments of icebergs by applying the mean brightness filter to all segments. Icebergs commonly show higher backscatter intensity compared to the surrounding sea water or sea ice (Silva and Bigg, 2005; Young et al., 1998; Mazur et al., 2017; Wesche and Dierking, 2012). According to Mazur et al. (2017), we can identify iceberg segments as the segments satisfying the following equation:

$$\gamma > -0.2\,\alpha \qquad (2)$$

where γ is the backscatter of SAR images, and α is the incidence angle of the SAR. When we employ this equation, we can successfully distinguish the target iceberg from the surrounding area (Figure 2e and 2f).
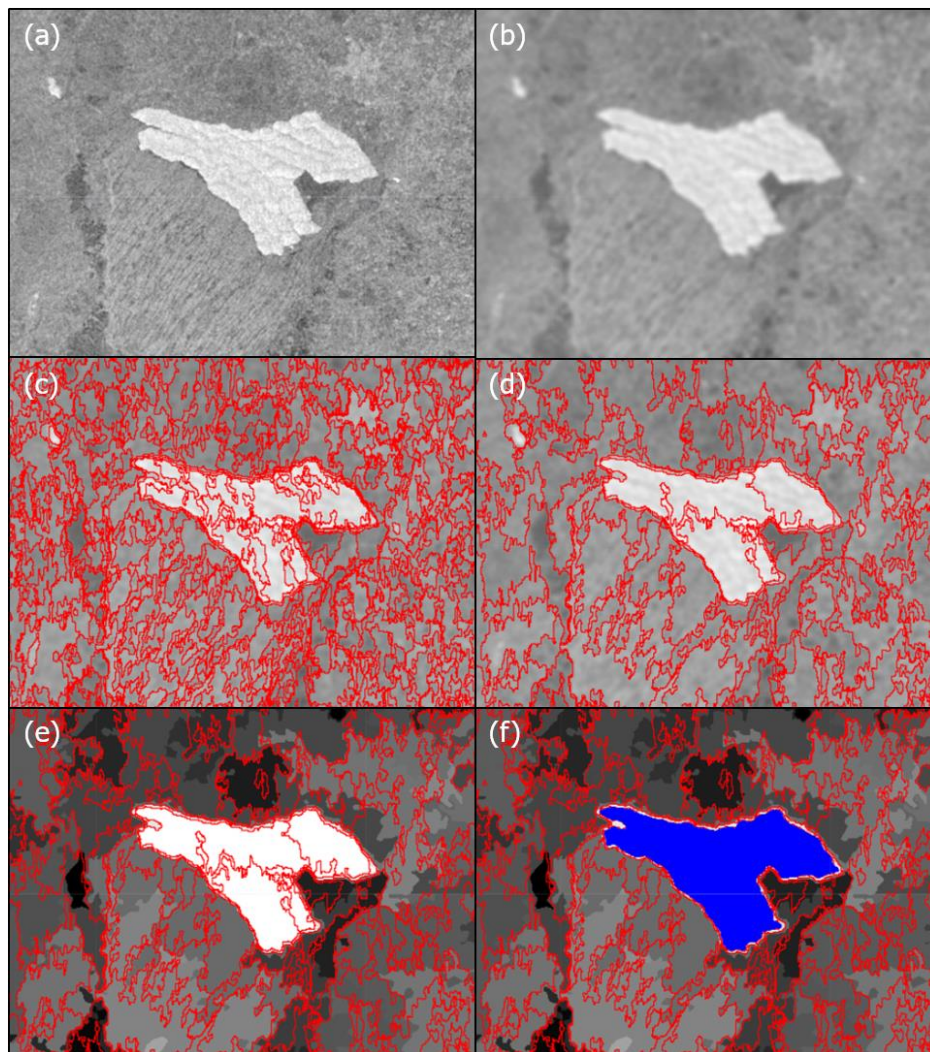
160

Figure 2. An example of the segmentation result for different levels: (a) original image (22 May 2019), (b) smoothed image by Gaussian filter, (c) Segmented image (seed = 40), (d) Segmented image (seed = 80), (e) backscatter ratio (= γ/α) image with segmented result, (f) segments identified as iceberg (blue polygon). Segmentation and other processing shown in (c)-(f) are based on the smoothed image in (b).

165

3.2. Iceberg tracking

In order to automatically detect and track only the target iceberg among multiple icebergs, we adopt a feature extraction method based on the centroid distance function (Mingqiang et al., 2008; Hasim et al., 2016; Arjun and Mirnalinee, 2015). As described in Figure 3, the automated iceberg tracking process consists of the following steps: (1) We manually digitize the polygon

170   of the reference iceberg from a Sentinel-1 image and calculate the distances from the iceberg centroid for all iceberg pixels. We make a histogram of these centroid distances for all pixels in the iceberg; this centroid distance histogram (CDH) represents the area and shape of the iceberg. (2) We search for an available Sentinel-1 image of the next day, within a 25 km radius from the reference iceberg in the current image. If the image for the next day is not available, the search radius is extended by 25 km each

day until a Sentinel-1 image is found (Figure 4a). (3) Once a Sentinel-1 image is found, all candidate icebergs are detected by the

175   same processes as described in 3.1. (4) We calculate the CDHs for all detected icebergs. (5) By comparing the similarities of the

CDHs between these icebergs and the reference iceberg, we determine which iceberg is the target iceberg for that day. The

similarity of CDH between iceberg A and reference iceberg ($r(A, \text{ref})$) is calculated by Equation 3.

$$r(A, \text{ref}) = \left(1 - \frac{\sum_{i=1}^{m} |N_A(i) - N_{ref}(i)|}{\sum_{i=1}^{m} N_{ref}(i)} \right) \times 100 \ (\%) \qquad (3)$$

where m is the bin size of the histogram, $N_A(i)$ and $N_{ref}(i)$ is the number of pixels in the i-th bin for iceberg A and reference

180   iceberg, respectively. We select the iceberg showing similarity greater than 80 % with the reference iceberg (Figure 4b-4d). If

multiple icebergs show similarity above 80 % with the reference iceberg, we select the iceberg with the highest similarity as the

target iceberg. Once the target iceberg is determined, the centroid of this iceberg becomes the center of search radius for the next

day in the second step. However, if the target iceberg is not detected, we return to the second step, expand the search radius, and

repeat the same steps until the target iceberg is detected (Figure 3).

185   It is worth noting that for some days, when a significant mass of the iceberg breaks from the iceberg, the shape of the

iceberg changes considerably. In these cases, the initial CDH would no longer be representative of the iceberg and a new reference

iceberg would have to be manually set. Three examples of these manual reference adjustments are days 18 March 2018, 25 March

2019, and 17 January 2020. In addition, if a Sentinel image is not found for more than five successive days, the search radius

becomes too large to be processed in the limited memory of GEE. In that case, we must manually find the next available Sentinel

190   image and day, and 40 images are manually found in this study. Thus, for processing total 433 images, 43 manual interventions (3

manual reference adjustments + 40 manual image search) are required (i.e. ~90 % of the total processes are automated). Because

of this need of occasional human intervention, we call our overall procedure semi-automated.

1. Digitize reference iceberg &
Create reference centroid distance
histogram (CDH)

Reference
CDH

2. Is there any
available image for the next
day within search
radius?

NO

YES

25 km

3. Detect all icebergs

1) SNIC image segmentation
2) Ratio threshold ($\gamma/\alpha > 0.2$)

25 km
* n day

Detected iceberg
becomes the center
for the next search

Expand search radius
(+25 km/day)

4. Calculate the similarities of CDH
between all detected icebergs and
the reference iceberg

YES

5. Is the target
iceberg detected?
(similarity > 80 %)

NO

Reference
2019-04-10

Similarity = 88.39%

N

Distance from the centroid (m)

Figure 3. Flow chart illustrating the steps of the semi-automated procedure for iceberg detection and tracking. Details are explained in the text (section 3.2).
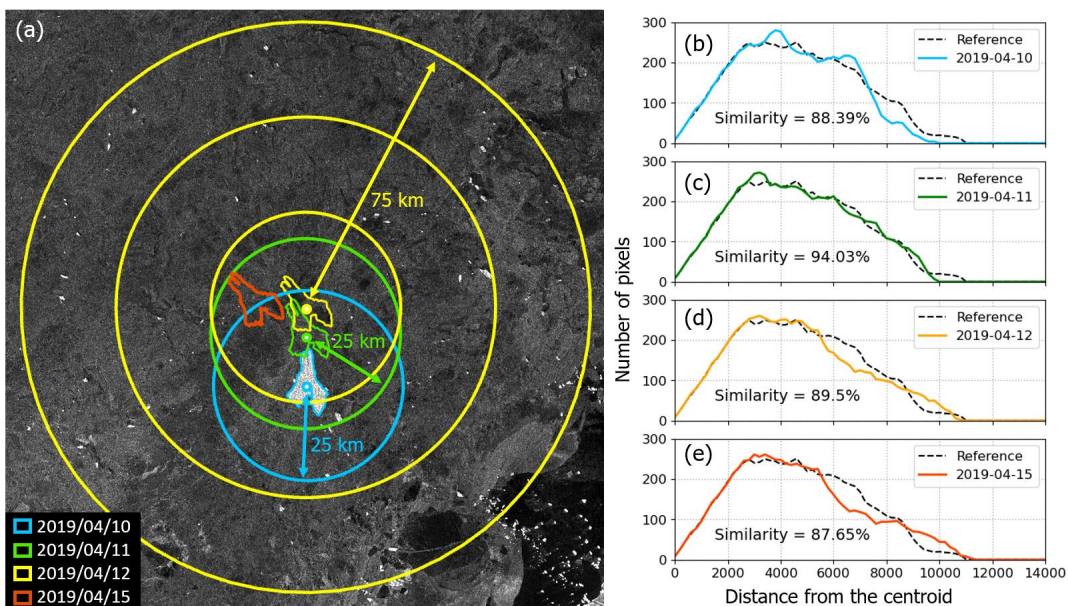
Figure 4. Tracking of the iceberg from 10 April 2020 to 15 April 2020. (a) Location of detected iceberg and search radius for each day, and centroid distance histograms (CDHs) of the target iceberg for (b) 10 April 2019, (c) 11 April 2019, (d) 12 April 2019, and (e) 15 April 2019.

3.3. Calculation of iceberg thickness

The freeboard of the iceberg (F) is defined as the difference between the heights of the iceberg body (H) and the sea surface heights (H_{ssh}) by the following equation:

$$F = H - H_{ssh} \quad (4)$$

For the CryoSat-2 data, we use the sea surface heights from the Level 2 SAR and SIN products, and for the ICESat-2 data, we use the sea surface heights from the ICESat-2 ATL10 sea ice freeboard products. We subtract these sea surface heights from the height measurements of the iceberg. Then the thickness of the iceberg (Z) can be roughly estimated from the freeboard by using Equation 5:

$$Z = \frac{\rho_w}{\rho_w - \rho_i}(F - \delta) + \delta \quad (5)$$

where ρ_w and ρ_i is the density of water and ice, respectively, and δ is the thickness correction of the upper firn layer. Here we assume 1,025 kg/m^3 and 915 kg/m^3 of seawater and ice density, respectively (Griggs and Bamber, 2011; Chuter and Bamber, 2015; Zhang et al., 2020), and 15 m of typical firn layer correction (Griggs and Bamber, 2011; Lythe and Vaughan, 2001).

4. Results and Discussion

4.1. Area variations of the iceberg

The iceberg area is retrieved by using our semi-automated iceberg tracking method (Figure 5a). We find three noteworthy

220   periods, all in summers or end-of-summers, when large reductions of the iceberg area are observed: (1) February-March 2018, (2) December 2018-March 2019, and (3) December 2019-March 2020 (gray shaded areas in Figure 5). We observe that a significant portion of the iceberg split away from the main iceberg during these periods. Except for these summer months, the area of the iceberg remained relatively constant or decreases gradually during the journey. Initially, from April 2017 to February 2018, the iceberg area remained at a nearly constant value of 105-107 km^2. The area then decreased rapidly to 95 km^2 around February-

225   March 2018. From then onwards the iceberg's area decreased gradually, falling under 90 km^2 around December 2018 to March 2019. The iceberg area then remained nearly constant at about 84 km^2 during April-November 2019 until it started to decrease again and eventually broke down into several smaller pieces in December 2019-March 2020.

         Although our iceberg tracking method extracts a good monthly mean trend of the iceberg area, there are several anomalous estimates of the individual area at a daily level (Figure 5a). One cause for this is the nearby small icebergs. We observe a number

230   of small icebergs around the coastal Amundsen Sea region, and they are sometimes adjacent to the iceberg B43. In this case, our iceberg-detecting algorithm recognizes them as a single iceberg body, which leads to overestimation of the iceberg area. Second, although we assume a high radar backscatter from the iceberg, this backscatter can vary by sensor incidence angle, iceberg surface, and weather conditions. The variations in backscatter of the iceberg can cause uncertainties in area estimation. In addition, if sea ice has a high backscatter, the similar backscatter between sea ice and the iceberg makes it difficult to distinguish the exact

235   boundary between them (Mazur et al., 2017). Finally, we need to consider the spatial uncertainties introduced when SAR images are projected into the map coordinates and are resampled into 40 m resolution.

         We compare the area changes with the ancillary meteorological data (Figure 5b-5d). It is noted that three split-up events occurred only in lower SIC areas and during higher air temperatures (Figure 5b and 5c). In higher SIC areas, the iceberg remains relatively stable because it is surrounded by sea ice. However, when SIC decreases and the iceberg is exposed to open water, the

240   interaction between waves and the iceberg can trigger the breakup of the iceberg (England et al., 2020; Scambos et al., 2008; Wagner et al., 2014). Given that this breakup mechanism is somewhat related to the water temperature and waves (Wagner et al., 2014), we deduce that SIC and temperature can have substantial impacts on the breakup events. In particular, the iceberg was completely broken into several small pieces in March 2020, after being continually exposed to open water since December 2019. There is a possibility that the rising wave heights during this period accelerate the breakup event (Figure 5d) (MacAyeal et al.,

245   2006). Nevertheless, considering the complexity of the breakup mechanism, it is challenging to clearly determine what caused the breakup of the iceberg B43.
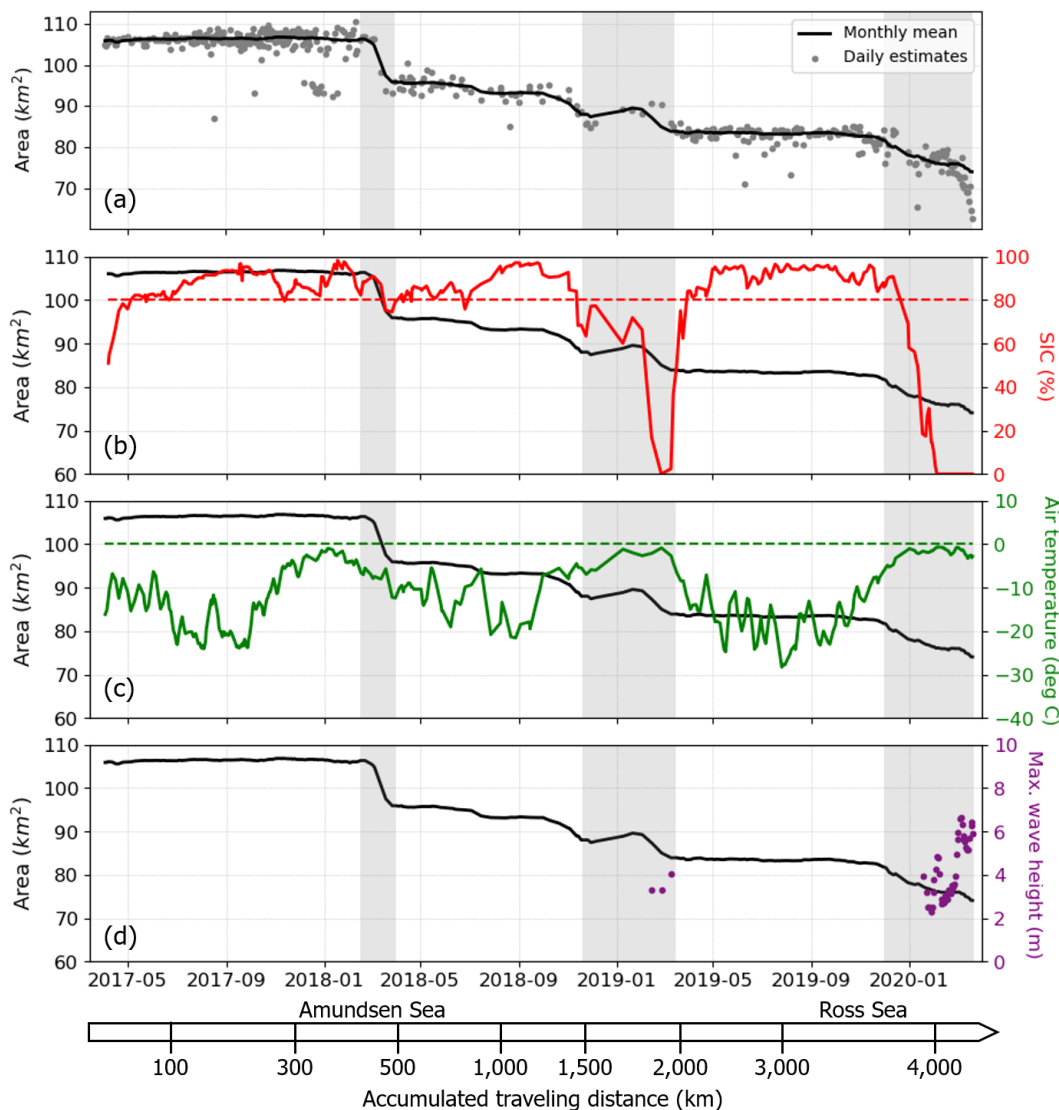
Figure 5. (a) Temporal changes of the iceberg area from April 2017 to March 2020. Comparison of area changes of the iceberg (black line) with (b) sea ice concentration (SIC) (red), (c) air temperature (green), and (d) maximum wave height (purple) from ERA5. Wave heights are not calculated for unmarked periods because the high SIC effectively dampens waves. Gray shaded areas indicate the split-off events of the iceberg.

4.2. Trajectory of the iceberg

The trajectory of iceberg B43 resulted from the semi-automated iceberg tracking is shown with solid colored circles in Figure 6. The trajectory agrees well with that from the National Ice Center (NIC) iceberg archive which is reproduced with a black dashed line in Figure 6. In contrast to our semi-automated tracking procedure, the NIC trajectory is manually retrieved by ice analysts every week using a combination of SAR, visible, and infrared remote sensing images (usicecenter.gov). As shown in Figure 6, B43 drifted from the Amundsen Sea in April 2017 into and through the Ross Sea in March 2020. The trajectory shows

260   that B43 initially drifted mainly toward the north and northwest until about April 2018, then towards the west until November
2018, then towards the southwest until June 2019, and finally towards the northwest until it broke off. This trajectory agrees with
the modeled trajectories of icebergs over the Amundsen Sea to the Ross Sea area (Gladstone et al., 2001; Merino et al., 2016;
Rackow et al., 2017).
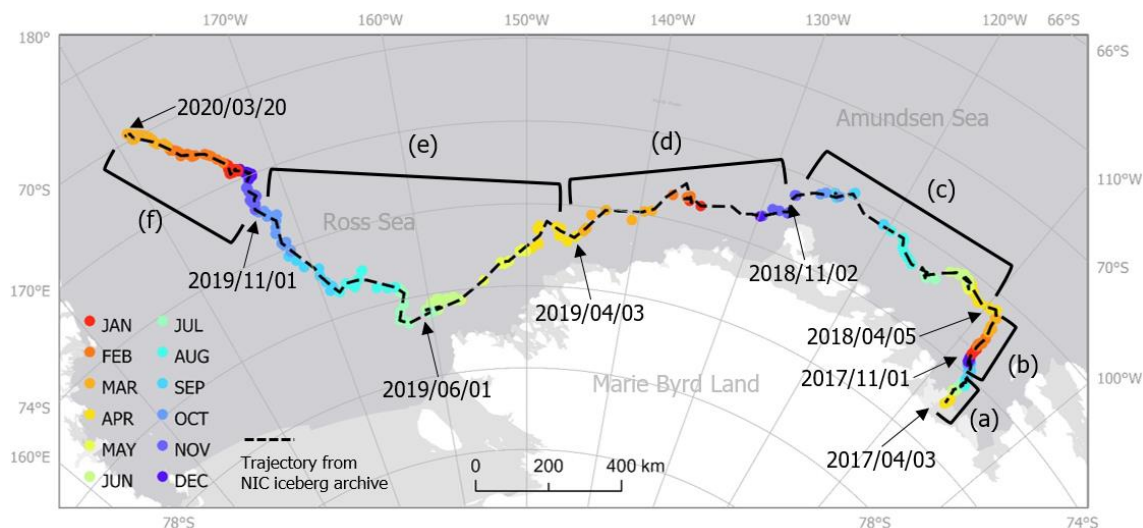
265

Figure 6. The trajectory of iceberg B43 from our semi-automatic algorithm (solid colored circles) and that obtained from the NIC
iceberg archive (black dashed line). The circle colors indicate the calendar month. The six square brackets labeled (a) to (f) indicate
track segments selected to investigate associations with ice motions and winds.

270   Figure 7 shows rose diagrams for iceberg velocity along with fields of average sea ice concentration, average ice motion,
and average wind velocity averaged for the six selected periods shown in Figure 6. Initially the iceberg moved relatively slowly.
From April 2017 to March 2018, a speed < 4 km/day was detected more than 90% of the time and similarly a speed < 2 km/day
was detected more than 75% of the time. The primary drift direction in this period was toward the west or northwest (50 % of the
time for April 2017-October 2017 and 60 % of the time for November 2017-March 2018), but occasionally it also drifted eastward
275   or northeastward (40 % of the time for April 2017-October 2017 and 25 % of the time for November 2017-March 2018). During
this period, iceberg B43 was mostly surrounded by slow and compacted sea ice (Figure 7a and 7b).
Figure 7. Multipanel plots with left-to-right columns respectively indicating rose diagrams of iceberg velocity, average sea ice concentration (SIC), average ice motion velocity, and average wind vector velocity. The rows correspond to the six averaging periods selected in Figure 6: (a) April 2017-October 2017, (b) November 2017-March 2018, (c) April 2018-October 2018, (d) November 2018-March 2019, (e) April 2019-October 2019, and (f) November 2019-March 2020. The entire track of the iceberg is indicated in all the maps (grey solid circles) as well as the track segments for each of the six periods (magenta solid circles).
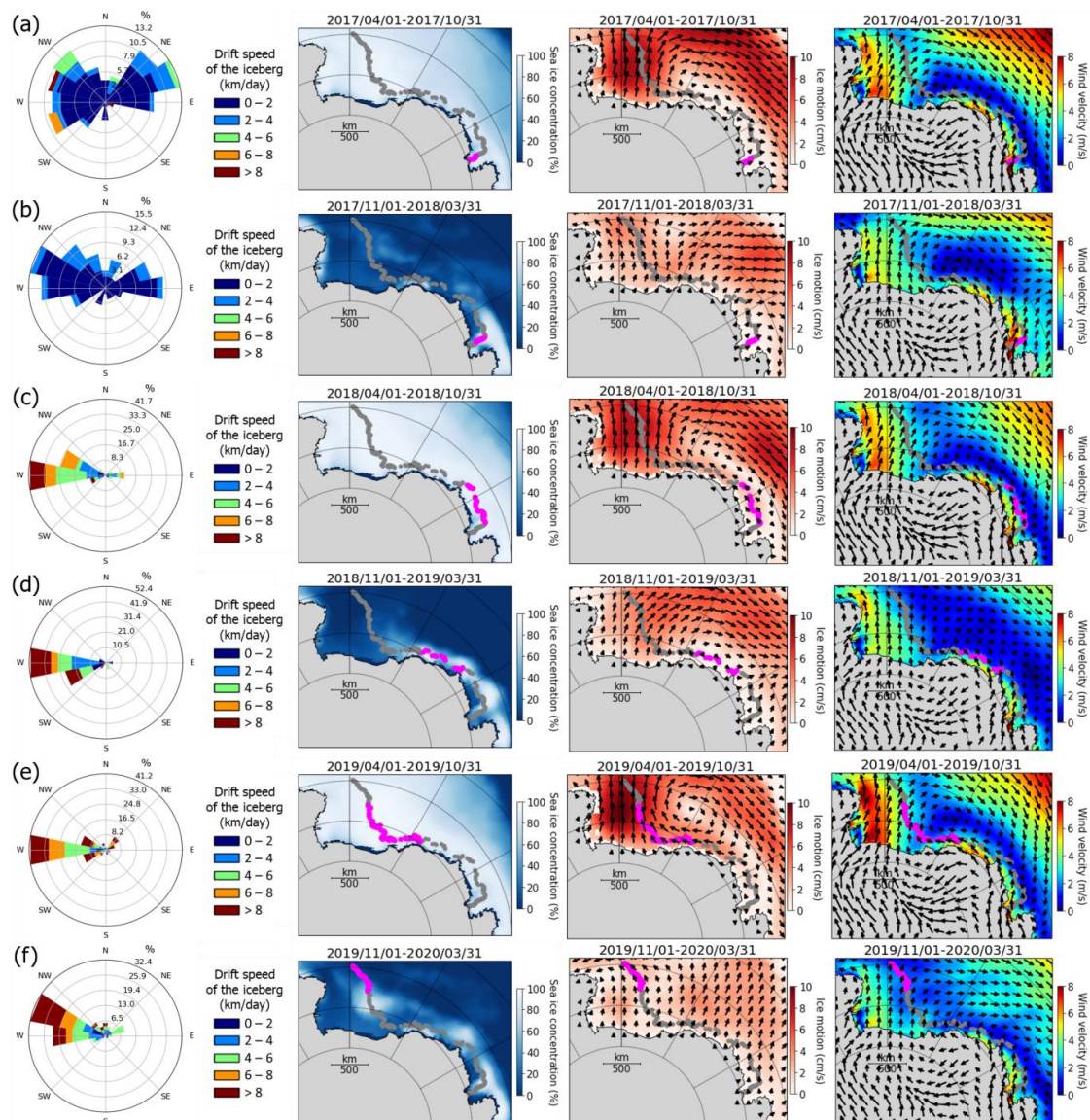
As B43 moved away from the starting point, however, its speed increased. From April 2018 to May 2019, the iceberg mainly moved westward parallel to the coastline more than 90 % of the time, which is consistent with the westward sea ice drift and wind velocity (Figure 7c-7e). During this journey from the Amundsen Sea to the eastern Ross Sea, the drift speed was faster than 4 km/day approximately 70 % of the time, and even greater than 8 km/day 10-40 % of the time. This increase of drift speed can mainly be attributed to the faster sea ice movement in this region compared to the starting point in the Amundsen Sea.

When B43 reached the Ross Sea (June 2019), it started to drift more in a northwestward direction (Figure 7e and 7f).

From April 2019 to October 2019 the iceberg drifted at its fastest speed as it passed through an area with the fastest sea ice motion (Figure 7e). It is also noted that the directional change from westward to northwestward during this period agrees with the direction of sea ice movement and wind direction in this region (Figure 7e). It is generally known that sea ice starts to move faster from this

295 region because sea ice is thinner in the Ross Sea compared to the Amundsen Sea, so sea ice is more affected by wind forcing (DeLiberty et al., 2011). Although the drift speed slightly decreased after November 2019, the iceberg was still observed to drift at > 8 km/day around 30% of the time for the last five months (Figure 6f). During the last five months, sea ice may have had less impact on the drift of B43 because it was surrounded by thinner sea ice (DeLiberty et al., 2011) or open water.

    Figure 8 compares the drift speed and the direction of the iceberg with SIC, wind velocity, and sea ice motion. Here we

300 merely focus on the qualitative comparison of the drift direction and speed with other climatological data. Considering that this iceberg moved along with highly compacted sea ice during most of its journey (SIC > 80 %, Figure 8a), the movement of the iceberg is likely to be related to the sea ice drift and wind velocity (Lichey and Hellmer H., 2001; Schodlok et al., 2006). Wind velocity and ice motion generally show similar variations for each other, and they both show substantial correlation with the iceberg drift (Figure 8b-8e). However, the impact of wind or sea ice drift on the iceberg drift could vary depending on the season, location,

305 SIC, and ocean current.

    Although we do not directly analyze ocean current data here due to the lack of reliability and availability of ocean current data under high-concentration sea ice, ocean current would account for a significant part of the iceberg drift because about 80-90 % of the iceberg is under the sea surface. Hence, the westward drift of this iceberg mainly represents the sea current along the Amundsen Sea to the Ross Sea. In the coastal regions of the Amundsen Sea and the Ross Sea, the ocean circulation is dominated

310 by the westward Antarctic Coastal Current (ACoC) which is mainly driven by wind stress and buoyancy (Whitworth III et al., 1985; Orsi et al., 1995; Mathiot et al., 2011; Kim et al., 2016; Stern et al., 2016).
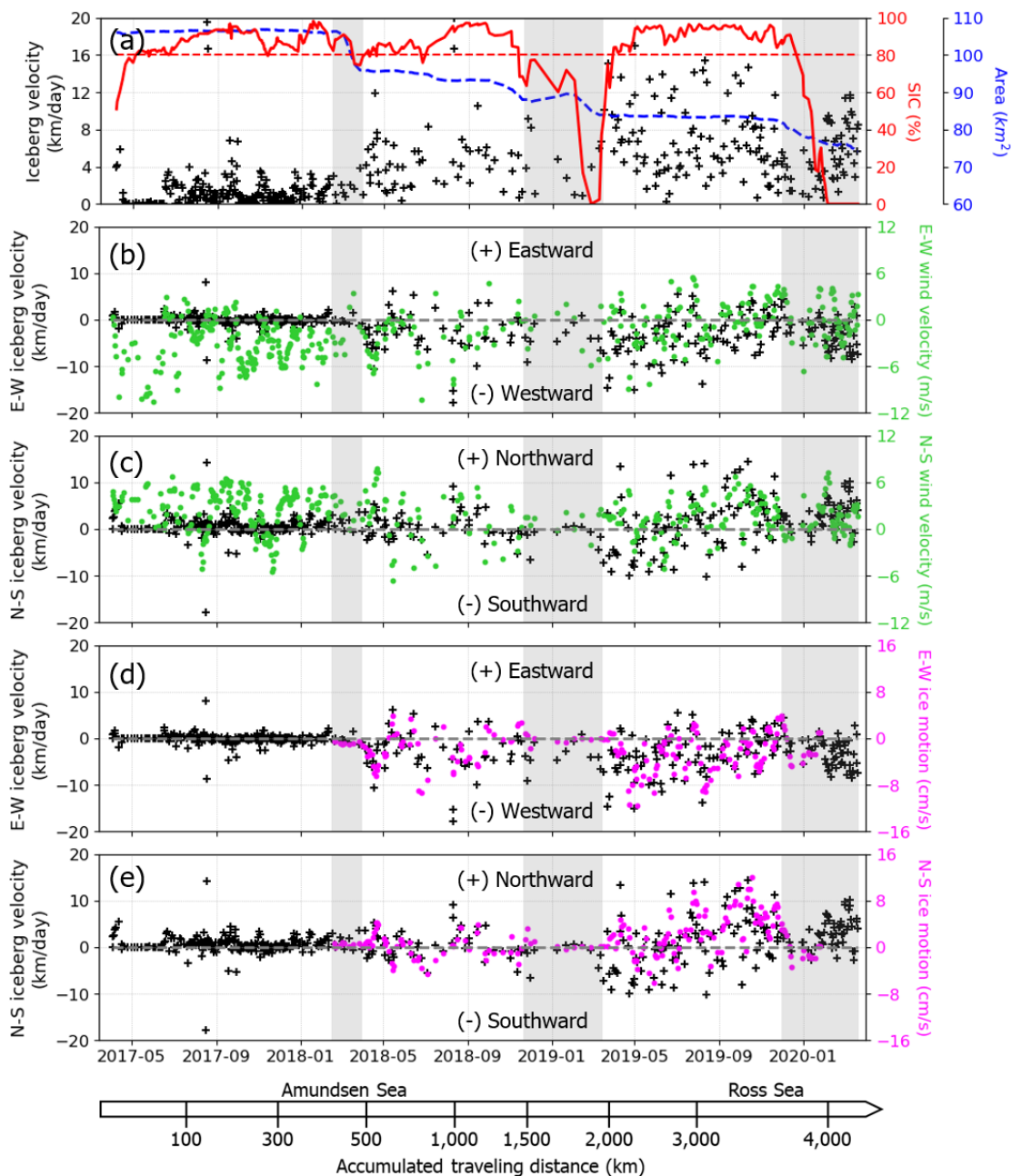
Figure 8. (a) Drift speed of the iceberg (black crosses), SIC (red solid line), and area changes (blue dashed line); (b) east-west
315 velocity of both the iceberg (black crosses) and the wind (green circles); (c) north-south velocity of both the iceberg (black crosses)
and the wind (green circles); (d) east-west velocity of both the iceberg (black crosses) and sea ice motion (magenta circles); (e)
north-south velocity of both the iceberg (black crosses) and sea ice motion (magenta circles). Gray shaded areas indicate the split-
off events of the iceberg.

320

4.3. Freeboard and thickness of the iceberg

To estimate the freeboard and thickness of the iceberg, we search for coincident CryoSat-2 and ICESat-2 tracks overlapping with the iceberg. We find one overlapping CryoSat-2 track and four overlapping ICESat-2 tracks that can be used to estimate the freeboard of the iceberg (Table 1). Although there are time differences between the Sentinel-1 images and the altimeter measurements, we conclude that these CryoSat-2/ICESat-2 tracks include the heights of the iceberg by comparing the drift of the iceberg and the height measurements. For example, Figure 9 shows the Sentinel-1 image on 31 March 2019, and the CryoSat-2 track on the same day. Although the higher points of CryoSat-2 do not exactly correspond to the iceberg in the Sentinel-1 image due to the time differences between the two datasets (around 14 hours), we can assume that these higher points represent the surface of the iceberg when the movement of the iceberg is considered. In particular, in the Sentinel-1 image, we cannot see any potential 40 m-height objects except the iceberg. Furthermore, near the iceberg, the CryoSat-2 points are off the straight ground track line, which indicates that there is an object different from the surrounding sea ice or open water. Since the retracking algorithm of the CryoSat-2 SIN product may emphasize a late-returned signal (Wingham et al., 2006), the radar signal from the edge of the iceberg can be biased to the non-iceberg area. Therefore, we assume that the heights represent the surface heights for the iceberg, and the mean freeboard is 42.4 m for this date (Table 1).

While CryoSat-2 has only one coincident track with the iceberg, there are four coincident ICESat-2 tracks passing through the iceberg (Table 1). Figure 10 shows an example of the ICESat-2 ATL03 data on 29 November 2019, and the Sentinel-1 image on the next day. Although they have time differences of about 24 hours, the heights of the ATL03 tracks are likely to represent the heights of the iceberg at the time of the Sentinel-1 image. It is interesting that ICESat-2 data describe the surface height of the iceberg in more detail with some ridges and valleys (Figure 10). This is attributed to a better spatial resolution of the ICESat-2 ATL03 product (17 m of footprint spaced by 0.7 m in the along-track direction) than the CryoSat-2 SAR or SIN product (~400 m of resolution in the along-track direction). In addition, the multiple tracks of ICESat-2 can be a considerable advantage for examining the shape of the iceberg surface.

As shown in Table 1, the iceberg freeboard is estimated to be greater than 50 m in November 2018, but less than 50 m from then on. There is not high confidence, however, that the thickness of this iceberg decreased during the drift because the number of height measurements is not sufficient to extract a significant trend. Moreover, since each track passed through a different part of the iceberg, the heights also depend on the sampling points where CryoSat-2 or ICESat-2 track were passing by. Nevertheless, we can deduce that the freeboard of this iceberg is within 30-60 m during the tracking period. This range of freeboard agrees with the previous estimates for other large icebergs over the Antarctic (Tournadre et al., 2015; Scambos et al., 2005; Romanov et al., 2012; Han et al., 2019). As shown in Table 1, this level of freeboard is equivalent to the iceberg thickness of 150-400 m. This implies that about 120-350 m of the iceberg thickness (i.e. 80-90 % fraction of the total thickness) is below the water surface. Thus, considering the average thickness (~265 m), initial area (~105 km^2), and 15 m firn layer of this iceberg, the melting of the entire iceberg body will contribute to approximately 24 Gt of freshwater input into the Southern Ocean. This amount of freshwater is equivalent to about 1 % of total annual freshwater flux in the Southern Ocean (Hammond and Jones, 2016).

Table 1. Freeboard and thickness of the iceberg estimated by ICESat-2 (IS2) and CryoSat-2 (CS2)

Date	Data	Latitude	Longitude	Freeboard (m)	Thickness (m)
2018-11-13	IS2 ATL03	-72.93	-127.58	52.59 ± 8.33	365 ± 78
2018-12-24	IS2 ATL03	-73.22	-131.70	37.21 ± 6.55	222 ± 61
2019-03-31	CS2 SIN	-74.62	-144.98	42.40 ± 5.88	270 ± 55
2019-11-29	IS2 ATL03	-72.12	-172.64	34.70 ± 8.90	199 ± 83
2020-02-07	IS2 ATL03	-71.13	-174.87	42.19 ± 3.86	268 ± 36
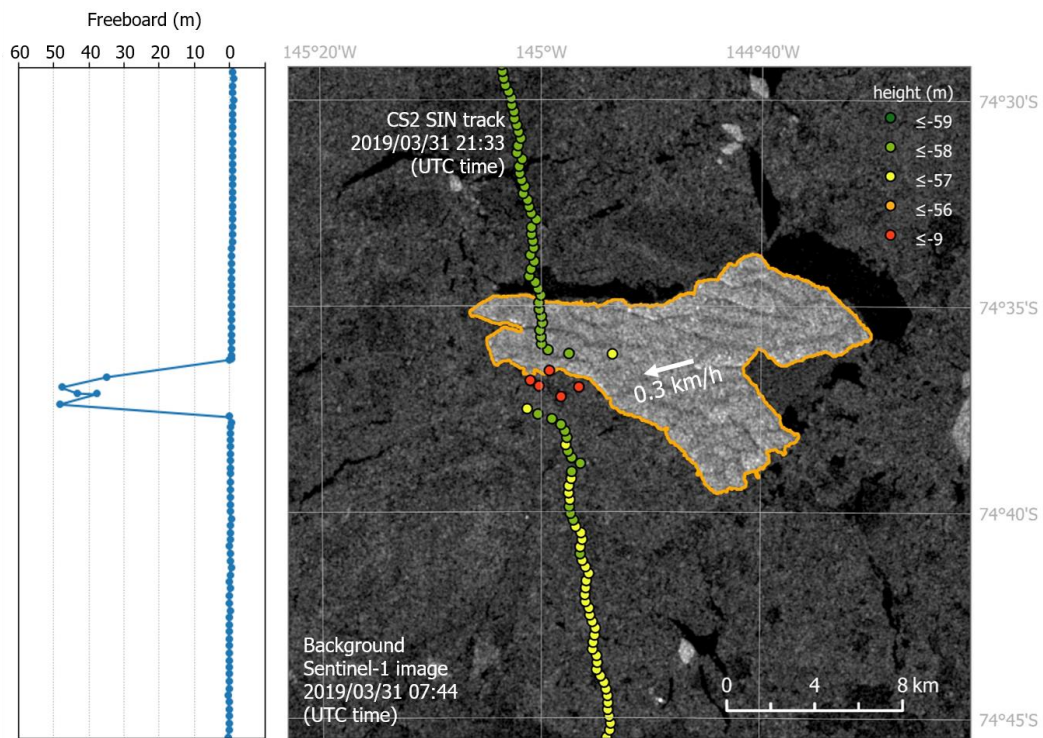
Figure 9. Freeboard measures from CS2 SIN track on 31 March 2019, and Sentinel-1 image 14 hours before. Considering the drift
360 of the iceberg between the image and the CS2 SIN track, the highest points (red dots) are the intercepted points on the iceberg by
the CS2 SIN track.
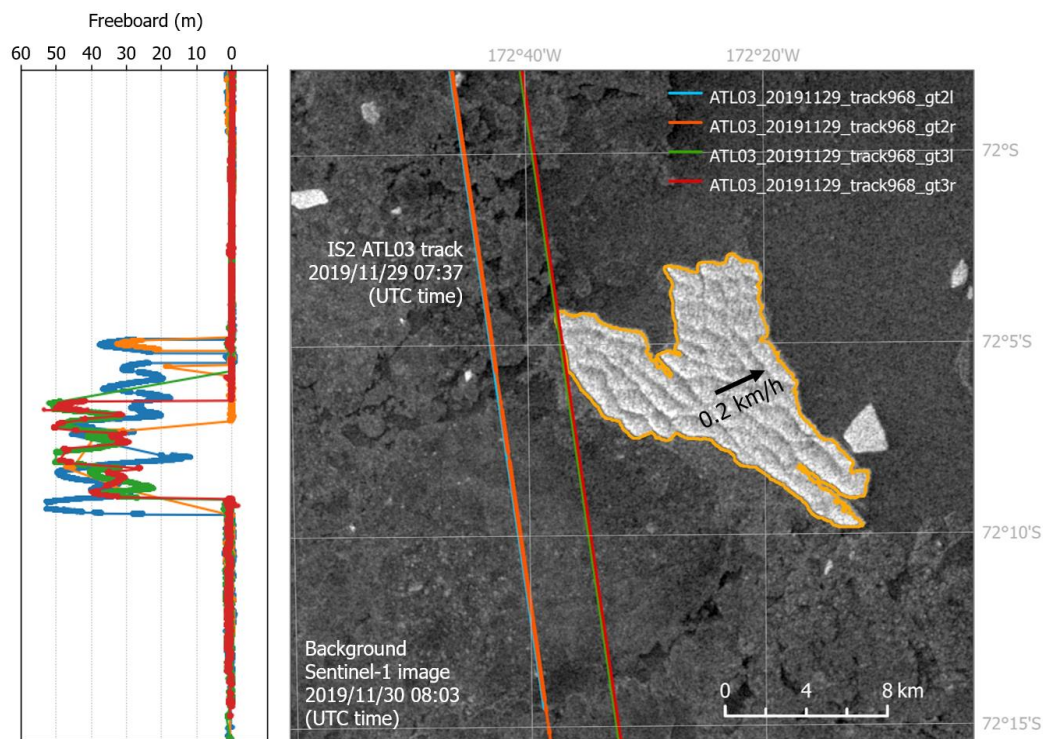
Figure 10. Freeboard measurements from ICESat-2 ATL03 tracks on 29 November 2019, and Sentinel-1 image on 30 November 2019 (about 24 hours later).

5. Conclusions

This study demonstrates for the first time the potential of Google Earth Engine (GEE) for iceberg tracking in the Southern Ocean using Sentienl-1 SAR images. It presents a cloud-based computational method for tracking iceberg B43 from when it calved off in the Amundsen Sea until it broke up in the Ross Sea. First, iceberg B43 is detected by using a SNIC object-based image segmentation and backscatter threshold algorithm. Then, the trajectory of this iceberg is constructed by comparing its centroid distance histogram with those of icebergs in subsequent images. Although manual tracking was used for several dates due to memory limitations of GEE and occasional large changes in the iceberg shape, the method (with a ~90% automation) was successful in tracking B43 for three years from April 2017 to March 2020.

Factors affecting the decrease in the area of iceberg B43 over time were studied by comparison with contemporaneous changes in environmental variables from ERA5 reanalysis data and NSIDC sea ice motion data. First, in terms of SIC, we find that split-up events of the iceberg occurred with lower SIC and higher exposure to open water conditions. This suggests that wave action, as calculated in ERA 5, played a role in triggering the break-up of the iceberg. Our analysis suggests that higher water temperature and higher wave heights can also accelerate this break-up mechanism. In addition, we find that iceberg drift could be associated with sea ice drift or wind velocity. The speed and direction of the iceberg drift agrees with the variations of sea ice drift and winds in the Amundsen Sea and Ross Sea regions. Given that this iceberg is 150-350 m thick, with the majority of its volume underwater, the main contribution to the westward drift of the iceberg is thought to be the westward sea current (ACoC) from the coastal Amundsen Sea to the Ross Sea.

Predicting the behavior of icebergs (e.g. trajectory, speed, decay, and breakup) is a highly complex endeavor that depends
385   on many factors related to dynamic and thermodynamic interactions between ocean currents, the atmosphere, waves, sea ice, and
bottom topography (Stern et al., 2016; Rackow et al., 2017; Schodlok et al., 2006; Lichey and Hellmer H., 2001; Gladstone et al.,
2001). Thus, developing, validating, and calibrating models for predicting iceberg's variables would require a large and accurate
iceberg database containing the life history of many icebergs. The method presented here can be used for these purposes by taking
advantage of GEE's large data storage capability and high computing power. Indeed, GEE allowed us to process 433 Sentinel-1
390   SAR images in the cloud, taking only 10-30 seconds to process and analyze one day of data and only a few hours to process all
three years. Moreover, since all image-processing tools were provided by GEE, this approach was able to save time, cost, and
resources compared to a similar traditional tracking done in a local computer. Therefore, iceberg tracking based on Sentinel-1
images and the GEE platform would be an efficient option for tracking a large number of icebergs in the polar oceans.

To build a large database of icebergs using the GEE-based iceberg tracking approach presented in this paper, however,
395   two key limitations would need to be overcome. First, although the centroid distance histogram (CDH) based approach successfully
tracks iceberg B43 (an iceberg with a distinctive shape and large size), this method has limitations in tracking small icebergs that
share similar shapes or areas. Indeed, we attempted unsuccessfully to track the small pieces of B43 when it broke up (Figure 1c)
because these pieces have similar CDHs. Second, our tracking algorithm is not fully-automated. In this study, instead of defining
the detected iceberg from the previous day as the reference for the next-day tracking, we defined the reference iceberg at the initial
400   digitizing step and use this reference for all the following steps. Although this approach enables us to avoid tracking errors caused
by temporary anomalies (e.g. impacts of surrounding small icebergs), it prevents our algorithm from detecting sudden changes in
the iceberg shape or area. By overcoming these limitations, fully-automated tracking of small icebergs would be possible and a
large and accurate iceberg database could be constructed.

405   *Code and data availability.* Python code for this GEE-based semi-automated iceberg tracking is available at:
https://github.com/YoungHyunKoo/GEE_iceberg_tracking.git.

Author contributions. YK designed the research, conducted programming and analysis, created figures, and drafted the initial
manuscript. HX, SA, AM, GM, CH contributed to writing and editing of the manuscript.
410

Competing interests. The authors declare that they have no conflict of interest.

Acknowledgments. We would like to thank the European Space Agency (ESA) for processing and providing Sentinel-1 data and
GEE for proving the cloud computation capability. Additional data: ECMWF, CryoSat-2, and ICESat-2 data from ESA and NASA
415   are acknowledged here.

Financial support. This study is funded by NASA (80NSSC18K0843 and 80NSSC19M0194) and NSF (1835784) grants.

References

420   Achanta, R. and Süsstrunk, S.: Superpixels and polygons using simple non-iterative clustering, Proc. - 30th IEEE Conf. Comput.
        Vis. Pattern Recognition, CVPR 2017, 2017-Janua, 4895–4904, https://doi.org/10.1109/CVPR.2017.520, 2017.
Achanta, R., Shaji, A., Smith, K., Lucchi, A., Fua, P., and Süsstrunk, S.: SLIC Superpixels Compared to State-of-the-Art
        Superpixel Methods, IEEE Trans. Pattern Anal. Mach. Intell., 34, 2274–2282,

https://doi.org/10.1109/TPAMI.2012.120, 2012.

425   Arjun, P. and Mirnalinee, T. T.: Affine invariant compact centroid distance shape descriptor for image retrieval, Appl. Math. Sci., 9, 2325–2335, https://doi.org/10.12988/ams.2015.53214, 2015.

Biddle, L. C., Kaiser, J., Heywood, K. J., Thompson, A. F., and Jenkins, A.: Ocean glider observations of iceberg-enhanced biological production in the northwestern Weddell Sea, Geophys. Res. Lett., 42, 459–465, https://doi.org/10.1002/2014GL062850, 2015.

430   Chuter, S. J. and Bamber, J. L.: Antarctic ice shelf thickness from CryoSat-2 radar altimetry, Geophys. Res. Lett., 42, 10721–10729, https://doi.org/10.1002/2015GL066515, 2015.

Clement, M. A., Kilsby, C. G., and Moore, P.: Multi-temporal synthetic aperture radar flood mapping using change detection, J. Flood Risk Manag., 11, 152–168, https://doi.org/10.1111/jfr3.12303, 2018.

Collares, L. L., Mata, M. M., Kerr, R., Arigony-Neto, J., and Barbat, M. M.: Iceberg drift and ocean circulation in the

435   northwestern Weddell Sea, Antarctica, Deep. Res. Part II Top. Stud. Oceanogr., 149, 10–24, https://doi.org/10.1016/j.dsr2.2018.02.014, 2018.

DeLiberty, T. L., Geiger, C. A., Ackley, S. F., Worby, A. P., and Van Woert, M. L.: Estimating the annual cycle of sea-ice thickness and volume in the Ross Sea, Deep. Res. Part II Top. Stud. Oceanogr., 58, 1250–1260, https://doi.org/10.1016/j.dsr2.2010.12.005, 2011.

440   Denbina, M. and Collins, M. J.: Iceberg detection using simulated dual-polarized Radarsat Constellation data, Can. J. Remote Sens., 40, 165–178, https://doi.org/10.1080/07038992.2014.945517, 2014.

DeVries, B., Huang, C., Armston, J., Huang, W., Jones, J. W., and Lang, M. W.: Rapid and robust monitoring of flood events using Sentinel-1 and Landsat data on the Google Earth Engine, Remote Sens. Environ., 240, 111664, https://doi.org/10.1016/j.rse.2020.111664, 2020.

445   England, M. R., Wagner, T. J. W., and Eisenman, I.: Modeling the breakup of tabular icebergs, Sci. Adv., 6, 1–9, https://doi.org/10.1126/sciadv.abd1273, 2020.

ESA: CryoSat-2 Product Handbook, 2019.

Frost, A., Ressel, R., and Lehner, S.: Automated Iceberg Detection Using High-Resolution X-Band SAR Images, Can. J. Remote Sens., 42, 354–366, https://doi.org/10.1080/07038992.2016.1177451, 2016.

450   Gladstone, R. M., Bigg, G. R., and Nicholls, K. W.: Iceberg trajectory modeling and meltwater injection in the Southern Ocean, J. Geophys. Res. Ocean., 106, 19903–19915, https://doi.org/10.1029/2000jc000347, 2001.

Gorelick, N., Hancher, M., Dixon, M., Ilyushchenko, S., Thau, D., and Moore, R.: Google Earth Engine: Planetary-scale geospatial analysis for everyone, Remote Sens. Environ., 202, 18–27, https://doi.org/10.1016/j.rse.2017.06.031, 2017.

Griggs, J. A. and Bamber, J. L.: Antarctic ice-shelf thickness from satellite radar altimetry, J. Glaciol., 57, 485–498,

455   https://doi.org/10.3189/002214311796905659, 2011.

Hammond, M. D. and Jones, D. C.: Freshwater flux from ice sheet melting and iceberg calving in the Southern Ocean, Geosci. Data J., 3, 60–62, https://doi.org/10.1002/gdj3.43, 2016.

Han, H., Lee, S., Kim, J. I., Kim, S. H., and Kim, H. C.: Changes in a giant iceberg created from the collapse of the Larsen C Ice Shelf, Antarctic Peninsula, derived from Sentinel-1 and CryoSat-2 data, Remote Sens., 11, 1–14,

460   https://doi.org/10.3390/rs11040404, 2019.

Hasim, A., Herdiyeni, Y., and Douady, S.: Leaf Shape Recognition using Centroid Contour Distance, IOP Conf. Ser. Earth Environ. Sci., 31, https://doi.org/10.1088/1755-1315/31/1/012002, 2016.

Heiselberg, H.: Ship-iceberg detection & classification in sentinel-1 SAR images, 14, 235–241,

https://doi.org/10.12716/1001.14.01.30, 2020.

465   Howell, C., Youden, J., Lane, K., Power, D., Randell, C., and Flett, D.: Iceberg and ship discrimination with ENVISAT multi-
        polarization ASAR, Int. Geosci. Remote Sens. Symp., 1, 113–116, https://doi.org/10.1109/igarss.2004.1368958, 2004.

      Jin, Z., Azzari, G., You, C., Di Tommaso, S., Aston, S., Burke, M., and Lobell, D. B.: Smallholder maize area and yield mapping
        at national scales with Google Earth Engine, Remote Sens. Environ., 228, 115–128,
        https://doi.org/10.1016/j.rse.2019.04.016, 2019.

470   Kim, C. S., Kim, T. W., Cho, K. H., Ha, H. K., Lee, S. H., Kim, H. C., and Lee, J. H.: Variability of the Antarctic Coastal
        Current in the Amundsen Sea, Estuar. Coast. Shelf Sci., 181, 123–133, https://doi.org/10.1016/j.ecss.2016.08.004, 2016.

      Lane, K., Power, D., Chakraborty, I., Youden, J., Randell, C., McClintock, J., and Flett, D.: RADARSAT-1 synthetic aperture
        radar iceberg detection performance ADRO-2 A223, Int. Geosci. Remote Sens. Symp., 4, 2273–2275,
        https://doi.org/10.1109/igarss.2002.1026516, 2002.

475   Lasserre, F.: Simulations of shipping along Arctic routes: Comparison, analysis and economic perspectives, Polar Rec. (Gr.
        Brit)., 51, 239–259, https://doi.org/10.1017/S0032247413000958, 2015.

      Lea, J. M.: The Google Earth Engine Digitisation Tool (GEEDiT) and the Margin change Quantification Tool (MaQiT) –
        Simple tools for the rapid mapping and quantification of changing Earth surface margins, Earth Surf. Dyn., 6, 551–561,
        https://doi.org/10.5194/esurf-6-551-2018, 2018.

480   Li, T., Shokr, M., Liu, Y., Cheng, X., Li, T., Wang, F., and Hui, F.: Monitoring the tabular icebergs C28A and C28B calved from
        the Mertz Ice Tongue using radar remote sensing data, Remote Sens. Environ., 216, 615–625,
        https://doi.org/10.1016/j.rse.2018.07.028, 2018.

      Lichey, C. and Hellmer H., H. H.: Modeling giant-iceberg drift under the influence of sea ice in the Weddell Sea, Antarctica, J.
        Glaciol., 47, 452–460, https://doi.org/10.3189/172756501781832133, 2001.

485   Lopez-Lopez, L., Parmiggiani, F., Moctezuma-Flores, M., and Guerrieri, L.: SAR image observations of the A-68 iceberg drift,
        Cryosph. Discuss., 1–16, https://doi.org/10.5194/tc-2020-180, 2020.

      Lythe, M. B. and Vaughan, D. G.: BEDMAP: A new ice thickness and subglacial topographic model of Antarctica, J. Geophys.
        Res. Solid Earth, 106, 11335–11351, https://doi.org/10.1029/2000jb900449, 2001.

      MacAyeal, D. R., Okal, E. A., Aster, R. C., Bassis, J. N., Brunt, K. M., Cathles, L. Mac, Drucker, R., Flicker, H. A., Kim, Y. J.,
490   Martin, S., Okal, M. H., Sergienko, O. V., Sponsler, M. P., and Thom, J. E.: Transoceanic wave propagation links
        iceberg calving margins of Antarctica with storms in tropics and Northern Hemisphere, Geophys. Res. Lett., 33,
        https://doi.org/10.1029/2006GL027235, 2006.

      Mahdianpari, M., Salehi, B., Mohammadimanesh, F., Homayouni, S., and Gill, E.: The first wetland inventory map of
        newfoundland at a spatial resolution of 10 m using sentinel-1 and sentinel-2 data on the Google Earth Engine cloud
495   computing platform, Remote Sens., 11, https://doi.org/10.3390/rs11010043, 2019.

      Mahdianpari, M., Salehi, B., Mohammadimanesh, F., Brisco, B., Homayouni, S., Gill, E., DeLancey, E. R., and Bourgeau-
        Chavez, L.: Big Data for a Big Country: The First Generation of Canadian Wetland Inventory Map at a Spatial
        Resolution of 10-m Using Sentinel-1 and Sentinel-2 Data on the Google Earth Engine Cloud Computing Platform, Can.
        J. Remote Sens., 46, 15–33, https://doi.org/10.1080/07038992.2019.1711366, 2020.

500   Mandal, D., Kumar, V., Bhattacharya, A., Rao, Y. S., Siqueira, P., and Bera, S.: Sen4Rice: A processing chain for differentiating
        early and late transplanted rice using time-series sentinel-1 SAR data with google earth engine, IEEE Geosci. Remote
        Sens. Lett., 15, 1947–1951, https://doi.org/10.1109/LGRS.2018.2865816, 2018.

      Markus, T., Neumann, T., Martino, A., Abdalati, W., Brunt, K., Csatho, B., Farrell, S., Fricker, H., Gardner, A., Harding, D.,

Jasinski, M., Kwok, R., Magruder, L., Lubin, D., Luthcke, S., Morison, J., Nelson, R., Neuenschwander, A., Palm, S.,
505   Popescu, S., Shum, C. K., Schutz, B. E., Smith, B., Yang, Y., and Zwally, J.: The Ice, Cloud, and land Elevation
Satellite-2 (ICESat-2): Science requirements, concept, and implementation, Remote Sens. Environ., 190, 260–273,
https://doi.org/10.1016/j.rse.2016.12.029, 2017.

Martin, S., Drucker, R. S., and Kwok, R.: The areas and ice production of the western and central Ross Sea polynyas, 1992–
2002, and their relation to the B-15 and C-19 iceberg events of 2000 and 2002, J. Mar. Syst., 68, 201–214,
510   https://doi.org/https://doi.org/10.1016/j.jmarsys.2006.11.008, 2007.

Mathiot, P., Goosse, H., Fichefet, T., Barnier, B., and Gallée, H.: Modelling the seasonal variability of the Antarctic Slope
Current, Ocean Sci., 7, 455–470, https://doi.org/10.5194/os-7-455-2011, 2011.

Mazur, A. K., Wåhlin, A. K., and Kręzel, A.: An object-based SAR image iceberg detection algorithm applied to the Amundsen
Sea, Remote Sens. Environ., 189, 67–83, https://doi.org/10.1016/j.rse.2016.11.013, 2017.

515   Merino, N., Le Sommer, J., Durand, G., Jourdain, N. C., Madec, G., Mathiot, P., and Tournadre, J.: Antarctic icebergs melt over
the Southern Ocean: Climatology and impact on sea ice, Ocean Model., 104, 99–110,
https://doi.org/https://doi.org/10.1016/j.ocemod.2016.05.001, 2016.

Mingqiang, Y., Kidiyo, K., and Joseph, R.: A Survey of Shape Feature Extraction Techniques, https://doi.org/10.5772/6237,
2008.

520   Moctezuma-Flores, M. and Parmiggiani, F.: Tracking of the iceberg created by the Nansen Ice Shelf collapse, Int. J. Remote
Sens., 38, 1224–1234, https://doi.org/10.1080/01431161.2016.1275054, 2017.

Neumann, T. A., Martino, A. J., Markus, T., Bae, S., Bock, M. R., Brenner, A. C., Brunt, K. M., Cavanaugh, J., Fernandes, S. T.,
Hancock, D. W., Harbeck, K., Lee, J., Kurtz, N. T., Luers, P. J., Luthcke, S. B., Magruder, L., Pennington, T. A.,
Ramos-Izquierdo, L., Rebold, T., Skoog, J., and Thomas, T. C.: The Ice, Cloud, and Land Elevation Satellite – 2
525   mission: A global geolocated photon product derived from the Advanced Topographic Laser Altimeter System, Remote
Sens. Environ., 233, 111325, https://doi.org/https://doi.org/10.1016/j.rse.2019.111325, 2019.

Neumann, T. A., Brenner, A., Hancock, D., Robbins, J., Saba, J., Harbeck, K., Gibbons, A., Lee, J., Luthcke, S. B., and Rebold,
T.: ATLAS/ICESat-2 L2A Global Geolocated Photon Data, Version 3,
https://doi.org/https://doi.org/10.5067/ATLAS/ATL03.003, 2020.

530   Orsi, A. H., Whitworth, T., and Nowlin, W. D.: On the meridional extent and fronts of the Antarctic Circumpolar Current, Deep.
Res. Part I, 42, 641–673, https://doi.org/10.1016/0967-0637(95)00021-W, 1995.

Power, D., Youden, J., Lane, K., Randell, C., and Flett, D.: Iceberg detection capabilities of radarsat synthetic aperture radar,
Can. J. Remote Sens., 27, 476–486, https://doi.org/10.1080/07038992.2001.10854888, 2001.

Rackow, T., Wesche, C., Timmermann, R., Hellmer, H. H., Juricke, S., and Jung, T.: A simulation of small to giant Antarctic
535   iceberg evolution: Differential impact on climatology estimates, J. Geophys. Res. Ocean., 122, 3170–3190,
https://doi.org/https://doi.org/10.1002/2016JC012513, 2017.

Romanov, Y. A., Romanova, N. A., and Romanov, P.: Distribution of icebergs in the Atlantic and Indian ocean sectors of the
Antarctic region and its possible links with ENSO, Geophys. Res. Lett., 35, 1–5,
https://doi.org/10.1029/2007GL031685, 2008.

540   Romanov, Y. A., Romanova, N. A., and Romanov, P.: Shape and size of Antarctic icebergs derived from ship observation data,
Antarct. Sci., 24, 77–87, https://doi.org/10.1017/S0954102011000538, 2012.

Scambos, T., Sergienko, O., Sargent, A., MacAyeal, D., and Fastook, J.: ICESat profiles of tabular iceberg margins and iceberg
breakup at low latitudes, Geophys. Res. Lett., 32, 1–4, https://doi.org/10.1029/2005GL023802, 2005.

Scambos, T., Ross, R., Bauer, R., Yermolin, Y., Skvarca, P., Long, D., Bohlander, J., and Haran, T.: Calving and ice-shelf break-
545   up processes investigated by proxy: Antarctic tabular iceberg evolution during northward drift, J. Glaciol., 54, 579–591,
https://doi.org/10.3189/002214308786570836, 2008.

Scheuchl, B., Flett, D., Caves, R., and Cumming, I.: Potential of RADARSAT-2 data for operational sea ice monitoring, Can. J.
Remote Sens., 30, 448–461, https://doi.org/10.5589/m04-011, 2004.

Schodlok, M. P., Hellmer, H. H., Rohardt, G., and Fahrbach, E.: Weddell Sea iceberg drift: Five years of observations, J.
550   Geophys. Res. Ocean., 111, 1–14, https://doi.org/10.1029/2004JC002661, 2006.

Schwarz, J. N. and Schodlok, M. P.: Impact of drifting icebergs on surface phytoplankton biomass in the Southern Ocean: Ocean
colour remote sensing and in situ iceberg tracking, Deep. Res. Part I Oceanogr. Res. Pap., 56, 1727–1741,
https://doi.org/10.1016/j.dsr.2009.05.003, 2009.

Silva, T. A. M. and Bigg, G. R.: Computer-based identification and tracking of Antarctic icebergs in SAR images, Remote Sens.
555   Environ., 94, 287–297, https://doi.org/10.1016/j.rse.2004.10.002, 2005.

Silva, T. A. M., Bigg, G. R., and Nicholls, K. W.: Contribution of giant icebergs to the Southern Ocean freshwater flux, J.
Geophys. Res. Ocean., 111, 1–8, https://doi.org/10.1029/2004JC002843, 2006.

Singha, M., Dong, J., Zhang, G., and Xiao, X.: High resolution paddy rice maps in cloud-prone Bangladesh and Northeast India
using Sentinel-1 data, Sci. Data, 6, 1–10, https://doi.org/10.1038/s41597-019-0036-3, 2019.

560   Starr, A., Hall, I. R., Barker, S., Rackow, T., Zhang, X., Hemming, S. R., van der Lubbe, H. J. L., Knorr, G., Berke, M. A., Bigg,
G. R., Cartagena-Sierra, A., Jiménez-Espejo, F. J., Gong, X., Gruetzner, J., Lathika, N., LeVay, L. J., Robinson, R. S.,
Ziegler, M., Brentegani, L., Caley, T., Charles, C. D., Coenen, J. J., Crespin, J. G., Franzese, A. M., Han, X., Hines, S.
K. V., Jimenez Espejo, F. J., Just, J., Koutsodendris, A., Kubota, K., Norris, R. D., dos Santos, T. P., Rolison, J. M.,
Simon, M. H., Tangunan, D., van der Lubbe, H. J. L., Yamane, M., and Zhang, H.: Antarctic icebergs reorganize ocean
565   circulation during Pleistocene glacials, Nature, 589, 236–241, https://doi.org/10.1038/s41586-020-03094-7, 2021.

Stern, A. A., Adcroft, A., and Sergienko, O.: The effects of Antarctic iceberg calving-size distribution in a global climate model,
J. Geophys. Res. Ocean., 121, 5773–5788, https://doi.org/https://doi.org/10.1002/2016JC011835, 2016.

Torres, R., Snoeij, P., Geudtner, D., Bibby, D., Davidson, M., Attema, E., Potin, P., Rommen, B. Ö., Floury, N., Brown, M.,
Traver, I. N., Deghaye, P., Duesmann, B., Rosich, B., Miranda, N., Bruno, C., L'Abbate, M., Croci, R., Pietropaolo, A.,
570   Huchler, M., and Rostan, F.: GMES Sentinel-1 mission, Remote Sens. Environ., 120, 9–24,
https://doi.org/10.1016/j.rse.2011.05.028, 2012.

Tournadre, J., Bouhier, N., Girard-Ardhuin, F., and Rémy, F.: Large icebergs characteristics from altimeter waveforms analysis,
J. Geophys. Res. Ocean., 120, 1954–1974, https://doi.org/https://doi.org/10.1002/2014JC010502, 2015.

Tschudi, M., Meier, W. N., Stewart, J. S., Fowler, C., and Maslanik, J.: Polar Pathfinder Daily 25 km EASE-Grid Sea Ice Motion
575   Vectors, Version 4, https://doi.org/https://doi.org/10.5067/INAWUWO7QH7B, 2019.

Di Tullio, M., Nocchi, F., Camplani, A., Emanuelli, N., Nascetti, A., and Crespi, M.: Copernicus big data and google earth
engine for glacier surface velocity field monitoring: Feasibility demonstration on san rafael and san quintin glaciers, Int.
Arch. Photogramm. Remote Sens. Spat. Inf. Sci. - ISPRS Arch., 42, 289–294, https://doi.org/10.5194/isprs-archives-
XLII-3-289-2018, 2018.

580   Wagner, T. J. W., Wadhams, P., Bates, R., Elosegui, P., Stern, A., Vella, D., Abrahamsen, E. P., Crawford, A., and Nicholls, K.
W.: The "footloose" mechanism: Iceberg decay from hydrostatic stresses, Geophys. Res. Lett., 41, 5522–5529,
https://doi.org/10.1002/2014GL060832, 2014.

Wesche, C. and Dierking, W.: Iceberg signatures and detection in SAR images in two test regions of the Weddell Sea,

Antarctica, J. Glaciol., 58, 325–339, https://doi.org/10.3189/2012J0G11J020, 2012.

585   Wesche, C. and Dierking, W.: Near-coastal circum-Antarctic iceberg size distributions determined from Synthetic Aperture
Radar images, Remote Sens. Environ., 156, 561–569, https://doi.org/10.1016/j.rse.2014.10.025, 2015.

Whitworth III, T., Orsi, A. H., Kim, S.-J., Nowlin Jr., W. D., and Locarnini, R. A.: Water Masses and Mixing Near the Antarctic
Slope Front, https://doi.org/https://doi.org/10.1029/AR075p0001, January 1985.

Willis, C. J., Macklin, J. T., Partington, K. C., Teleki, K. A., Rees, W. G., and Rees, W. G.: Iceberg detection using ers-1
590   synthetic aperture radar, Int. J. Remote Sens., 17, 1777–1795, https://doi.org/10.1080/01431169608948739, 1996.

Wilson, K. J., Turney, C. S. M., Fogwill, C. J., and Blair, E.: The impact of the giant iceberg B09B on population size and
breeding success of Adélie penguins in Commonwealth Bay, Antarctica, Antarct. Sci., 28, 1–7,
https://doi.org/10.1017/S0954102015000644, 2016.

Wingham, D. J., Francis, C. R., Baker, S., Bouzinac, C., Brockley, D., Cullen, R., de Chateau-Thierry, P., Laxon, S. W., Mallow,
595   U., Mavrocordatos, C., Phalippou, L., Ratier, G., Rey, L., Rostan, F., Viau, P., and Wallis, D. W.: CryoSat: A mission
to determine the fluctuations in Earth's land and marine ice fields, Adv. Sp. Res., 37, 841–871,
https://doi.org/10.1016/j.asr.2005.07.027, 2006.

Young, N. W., Turner, D., Hyland, G., and Williams, R. N.: Near-coastal iceberg distributions in East Antarctica, 50-145°E,
Ann. Glaciol., 27, 68–74, https://doi.org/10.3189/1998aog27-1-68-74, 1998.

600   Zhang, M., Chen, F., Tian, B., Liang, D., and Yang, A.: High-frequency glacial lake mapping using time series of sentinel-
1A/1B sar imagery: An assessment for the southeastern tibetan plateau, Int. J. Environ. Res. Public Health, 17,
https://doi.org/10.3390/ijerph17031072, 2020.